Advances in Nano Research, *Vol. 13, No.3 (2022) 285-295*
https://doi.org/10.12989/anr.2022.13.3.285

Seismic response of NFRP reinforced RC frame with shape memory alloy components

Mohamad Motalebi Varkani[1], Mahmood Rabani Bidgoli[*1,2] and Hamid Mazaheri[1]

[1]*Department of Civil Engineering, Khomein Branch, Islamic Azad University, Khomein, Iran*
[2]*Department of Civil Engineering, Jasb Branch, Islamic Azad University, Jasb, Iran*

(*Received March 5, 2022, Revised June 14, 2022, Accepted June 15, 2022*)

Abstract. Creation of plastic deformation under seismic loads, is one of the most serious subjects in RC structures with steel bars which reduces the life threatening risks and increases dissipation of energy. Shape memory alloy (SMA) is one of the best choice for the relocating plastic hinges. In a challenge to study the seismic response of concrete moment resisting frame (MRF), this article investigates numerically a new type of concrete frames with nano fiber reinforced polymer (NFRP) and shape memory alloy (SMA) hinges, simultaneously. The NFRP layer is containing carbon nanofibers with agglomeration based on Mori-Tanaka model. The tangential shear deformation (TASDT) is applied for modelling of the structure and the continuity boundary conditions are used for coupling of the motion equations. In SMA connections between beam and columns, since there is phase transformation, hence, the motion equations of the structure are coupled with kinetic equations of phase transformation. The Hernandez-Lagoudas theory is applied for demonstrating of pseudoelastic characteristics of SMA. The corresponding motion equations are solved by differential cubature (DC) and Newmark methods in order to obtain the peak ground acceleration (PGA) and residual drift ratio for MRF-2%. The main impact of this paper is to present the influences of the volume percent and agglomeration of nanofibers, thickness and length of the concrete frame, SMA material and NFRP layer on the PGA and drift ratio. The numerical results revealed that the with increasing the volume percent of nanofibers, the PGA is enhanced and the residual drift ratio is reduced. It is also worth to mention that PGA of concrete frame with NFRP layer containing 2% nanofibers is approximately equal to the concrete frame with steel bars.

Keywords: concrete frame; drift ratio; seismic response; shape memory alloys; NFRP layer

1. Introduction

Among the important issues in the seismic design of concrete structures there is the discussion of ductility and energy dissipation. In buildings with a MRF system, most of the ductility at the end areas of the beams is provided by the formation of plastic joints created in large deformations during an earthquake. Due to the existence of residual deformation after the earthquakes in common concrete structures and the impossibility of exploiting them, the use of smart materials instead of longitudinal rebars in concrete elements, is essential. In addition, due to the disadvantages of concrete and the challenges in using concrete as one of the most widely used materials in civil works, researchers have tried to improve the properties of this material. Shape memory alloys are a type of smart metal material that exhibits distinctive behaviors and because of these characteristics have found wide applications in civil engineering (Moni 2011, Alam *et al.* 2011, Rojob *et al.* 2017, Elfeki and Youssef 2017, Oudah and El-Hacha 2018). With the discovery of smart alloys, researchers in recent years are studying the possibility of using these materials to improve the performance of concrete structures. These materials have exclusive properties, such as high service life, ultimate hardness in high deformations, possibility of removing residual strains by applying temperature, creating stress by applying temperature, stability of stress-strain behavior to about ten percent without leaving a residual strain, which can be used to reduce the damage of structures. There are two mechanisms for reversibility of deformations in memory materials. Memory effect (repair of residual strain by heat) and super-elastic behavior (residual strain repair by loading) which is caused by the conversion of austenite and martensite phases at different temperatures or by loading or unloading (Gur *et al.* 2017, Huang and Chang 2017). Due to their super-elasticity behavior, these alloys have high strain tolerance without leaving residual strain and they can be used in various parts of structures, especially to increase the structure's resistance against earthquakes. In general, it can be said that the dynamic capacity of the structure is effectively improved by the use of memory alloys compared to conventional structures, which is due to its reversibility and the ability to reduce the dynamic response. Moreover, in recent years, reinforcement and improvement of concrete structures performance with Fiber Reinforced Polymer (FRP) sheet has been considered due to its many advantages such as low weight ratio, easy to transport, increase the ductility and energy absorption capacity, especially under the influence of lateral loads (Ouyang *et al.* 2017, Yuan *et al.* 2020, Blazy and Blazy 2021). However, there are very few articles in the field of numerical analysis of concrete structures strengthened with nanofiber-reinforced polymers (NFRP).

*Corresponding author, Ph.D.,
E-mail: mahmood.rabanibidgoli@iau.ac.ir

ISSN: 2287-237X (Print), 2287-2388 (Online)

Therefore, in the following, several research about the use of SMA in concrete structures subjected to earthquakes are presented and then a number of articles about the mathematical modelling of the concrete structures reinforced with NFRP are stated.

Zafar and Andrawes (2015) studied the seismic behavior of SMA–FRP reinforced concrete frames under sequential seismic hazard. Their results showed that the superior performance of SMA–FRP composite reinforced MFR in terms of dissipation of energy and accumulation of lower residual drifts. Muntasir Billah and Shahria Alam (2016) proposed a new equation for predicting the plastic hinge length of SMA-RC bridge pier. They indicated that the plastic hinge length of SMA-RC pier increases when the axial load, aspect ratio and the yield strength of SMA rebar enhance. Lobo *et al*. (2017) numerically considered a reinforced concrete frame coupled with a variety of energy dissipation devices, namely viscous dampers, steel hysteretic dampers, and passive and semi-active SMA based devices. They stated that the passive solution with SMA and the steel hysteretic dissipators have not capability of satisfactorily reducing displacements. Pareek *et al*. (2018) considered the relocation of plastic hinge and cyclic performance of four Cu-Al-Mn SMA RC beams through an experimental-numerical study. They showed that the relocation of plastic hinge improves the strength, rigidity, and energy dissipation. Abou-Elfath (2018) studied the seismic performance characteristics of SMA reinforced concrete frames by performing a series of static pushover and dynamic earthquake analyses on typical framed structures. The performance parameters included the initial lateral stiffness, the energy dissipation capacity, the ductility ratios and the residual deformations both at the cross-section level and at the structure level. The results of this study showed that SMA-RC systems are characterized with excellent recentering behavior and poor levels of ductility ratio and energy dissipation ability. Navarro-Gómez and Bonet (2019) improved the seismic behaviour of reinforced concrete MRFs by means of SMA bars and ultra-high performance concrete. It is concluded that the combination of SMA and ultra-high performance concrete allow the behaviour factor to increase and residual drifts to decrease, which are advantages for both design and seismic behaviour. Hosseini *et al*. (2019) investigated the difference between the effect of Fe-SMA and carbon fiber reinforced polymer (CFRP) for prestressed strengthening of metallic structures. Nunes and Pedro (2019) explored the influence of the SMA constitutive model on the longitudinal seismic response of RC bridges. They numerically assessed the measure of the errors for numerical predictions with different constitutive models, peak, relative and residual displacements of four two-framed reinforced concrete bridges linked by SMA bars, subjected to seismic actions. They showed that the relative displacements are more sensitive to the adopted SMA model than the peak and residual displacements. Abreik (2020) introduced a new hybrid plastic hinge (HPH), which combines the steel and SMA bars within the critical sections to reduce construction costs and enhance the seismic performance of reinforced concrete frame building under sequence ground motions. Karimipour and Edalati (2020) considered the shear and flexural performance of low, normal and high-strength concrete beams reinforced with longitudinal SMA, glass fiber reinforced polymer (GFRP) and steel rebars. They concluded that GFRP and SMA rebars improve both maximum bending capacity and the deformation of specimens, however, the impact of SMA is higher than those manufactured with GFRP. Siddiquee *et al*. (2021) considered the seismic performance of concrete frame buildings reinforced with superelastic SMA rebar evaluated in terms of Collapse Margin Ratio (CMR). They compared their results with the performance of concrete frames reinforced with only regular steel rebar and found that an increase in collapse capacity for 3 and 8 story concrete frame structures using SMA versus steel rebar as reinforcement. Ding *et al*. (2021) considered the vibration performance of a shear frame structure equipped with SMA wires considering soil-structure interaction through finite element method. The study showed that the material and radiation damping of the soil-foundation interaction have a significant influence on the vibration control performance of SMAs. Lee *et al*. (2021) minimize the operational and repair costs of damaged plastic hinge region in concrete columns under earthquake loading by deriving an analytical expression for the plastic hinge length of rectangular concrete columns reinforced with nickel-titanium SMA bars based on the results from well-calibrated nonlinear finite element models.

The following articles are related to the experimental and numerical analysis of concrete elements strengthened with NFRP. Jeon *et al*. (2015) revealed he mechanical/ dynamic property of the CFRP to reduce the vibration/noise problems on rail slab. They fabricate the CFRP with the different weight fraction of carbon fiber and different fiber length. The flexural strength of the CFRP is measured using 3-point bending test. Safari Bilouei *et al*. (2016) investigated the nonlinear buckling of concrete columns armed with NFRP resting on foundation. Their results indicated that by reinforcing the concrete column with NFRP, the structure becomes stiffer and the buckling load increases with respect to concrete column armed with steel. Zamani and Rabani Bidgoli (2017) investigated the vibration of concrete foundations retrofit with NFRP layer resting on soil medium using sinusoidal shear deformation theory. They concluded that the frequency of the system enhances with increasing the NFRP thickness. Shariati Rad and Rabani Bidgoli (2017) studied the dynamic response of the NFRP strengthened concrete beam subjected to seismic ground excitation. The results indicated that applied NFRP layer decreases the maximum dynamic displacement of the structure up to 91 percent. Hajmohammad *et al*. (2018) investigated the seismic response of underwater fluid-conveying concrete pipes reinforced with NFRP layer during the Kube earthquake. The displacement filed of the structure is considered based on the sinusoidal shear deformation theory. The results showed that with increasing the thickness to radius ratio and volume percent of nano fiber and using NFRP layer, the dynamic deflection decreases. Mahjoobi and Rabani Bidgoli (2019) suggested a mathematical model for the dynamic response of sandwich

concrete foundation with NFRP layers at the top and bottom face sheets subjected to a blast load. Mahjoobi *et al*. (2021) examined the dynamic response of quadrilateral concrete foundation covered by NFRP layers at the top and bottom surfaces resting on soil medium subjected to blast load.

In the field of considering the other kinds of works on nanostructure, the porosity effect, different shear deformation theories and using novel materials, the following articles can be mentioned. Bekkaye *et al*. (2020) considered the bending and buckling of porous functionally graded plate under mechanical load using a refined trigonometric shear deformation theory. Al-Osta *et al*. (2021) studied the porosity effect on the hygro-thermo-mechanical bending response of an advanced functionally graded ceramic-metal plates supported by a two-parameter elastic foundation using an integral plate model. Kumar *et al*. (2021) applied a refined trigonometric higher-order shear deformation theory with the conjunction of nonlocal theory for the vibrational response of functionally graded porous nanoplate. Tahir *et al*. (2021) considered the Wave propagation in a porous functionally graded (FG) sandwich plate including a hygro-thermal medium. They used a simple four-unknown integral higher-order shear deformation theory and concluded that the temperature and moisture cause material expansions with additional stresses in the FG plate. Al- Hajlaoui *et al*. (2019) calculated the buckling load of functionally graded carbon nanotube-reinforced shells using a modified first order enhanced shell element formulation. The effects of power-law index on the nonlinear static behavior of the FGM shells were discussed by Hajlaoui *et al*. (2020a). Hajlaoui *et al*. (2020b) studied the static behavior of carbon nanotubes reinforced functionally graded shells using an efficient shell element with parabolic transverse shear strain.

A comprehensive review of the existing technical literature reveals that there is no research in the field of mathematical modelling of RC frames subjected to earthquake load covered with NFRP layer and SMA, simultaneously. This interesting topic is essential for designing and constructing of novel engineering structures. The use of these alloys in critical areas of the structure, such as the place where plastic joints are formed, reduces the permanent deformation after the earthquake. Hence, in this study, a concrete frame with NFRP layers and SMA is modeled using mathemtical relations of TASDT subjected to earthquake acceleration. The parameters of PGA and residual drift ratio are investigated based on DC-Newmark methods. The main contribution of this article is to study the influences of the volume percent and agglomeration of nanofibers, thickness and length of the concrete frame, SMA material and NFRP layer on the PGA and drift ratio.

2. Basic equations

Fig. 1 presents a concrete planar frame with SMA beam hinges and NFRP layers subjected to earthquake load. The thickness of the concrete and SMA are h_c, the thickness of NFRP layer is h_f, length of concrete beam and columns is L_1, L_4 and L_7, SMA beam length is L_{SMA}. The concrete

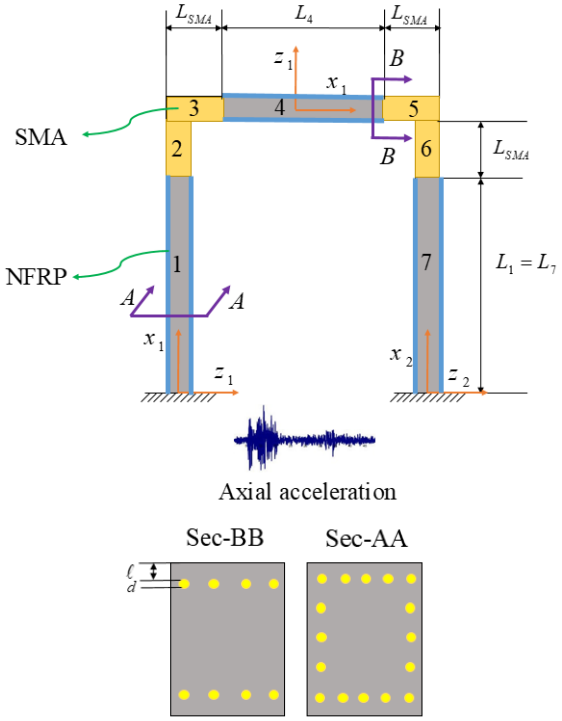

Fig. 1 Schematics of MRF with SMA beams and NFRP layers

beams are covered by NFRP layer and boundary condition of the structure is clamped-clamped. In addition, sections of A-A and B-B shows the configuration of steel bars in the concrete frame.

On the basis of tangential theory, the displacement field for the MRF may be given as (Simsek and Reddy 2013)

$$u(x,z,t) = u(x,t) - z\frac{\partial w(x,t)}{\partial x} + \underbrace{[tanh(z/h - (z/h)^3 - 0.8(z/h)^5)]}_{f(x)}\psi(x,t)\,, \tag{1}$$

$$v(x,z,t) = 0\,, \tag{2}$$

$$w(x,z,t) = w(x,t)\,, \tag{3}$$

where u and w are mid-plane dynamic displacements in the x and z directions, respectively,ψ is the rotation of cross section. The normal and shear strains for the MRF are:

$$\varepsilon_{xx} = \frac{\partial u}{\partial x} - z\frac{\partial^2 w}{\partial x^2} + f\frac{\partial \psi}{\partial x}, \tag{4}$$

$$\varepsilon_{xz} = cos\left(\frac{\pi z}{h}\right)\psi, \tag{5}$$

The stress-strain relations for the concrete elements, NFRP layers and SMA are:

$$(\sigma_{xx}^c, \sigma_{xx}^n, \sigma_{xx}^s) = (C_{11}^c, C_{11}^n, C_{11}^s)\varepsilon_{xx}, \tag{6}$$

$$(\sigma_{xz}^c, \sigma_{xz}^n, \sigma_{xz}^s) = (C_{55}^c, C_{55}^n, C_{55}^s)\varepsilon_{xz}, \tag{7}$$

where $C_{11}^k k = c,n,s$and $C_{55}^k k = c,n,s$are elastic constants

of concrete, NFRP and SMA. The Young's modulus of concrete, NFRP and SMA can be obtained by mixture rule, Mori-Tanaka (Jassas *et al*. 2019) and Hernandez-Lagoudas (Lagoudas *et al*. 2012) models, respectively as

$$E_{Concrete}|_{A-A}=\begin{cases}V_CE_C+V_SE_Sz=-\dfrac{h_c}{2}+d+\ell,\dfrac{h_c}{2}-d-\ell,\\ y=\dfrac{b}{2}-d-\ell,-\dfrac{b}{2}+d+\ell\\ E_Cotherwise\end{cases}$$
$$E_{Concrete}|_{B-B}=\begin{cases}V_CE_C+V_SE_Sy=\dfrac{b}{2}-d-\ell,-\dfrac{b}{2}+d+\ell\\ E_Cotherwise\end{cases} \quad (8)$$

$$E_{NFRP}=\frac{9KG}{3K+G}, \quad (9)$$

$$E_{SMA}(\xi)=\left[\frac{1}{E^A}+\xi\left(\frac{1}{E^M}-\frac{1}{E^A}\right)\right]^{-1}, \quad (10)$$

where the effective bulk modulus (*K*) and effective shear modulus (*G*) are defied in Appendix A based on Mori-Tanaka model. In addition, superscript "M" and "A" shows the martensite and austenite phases, respectively and ξ is martensitic volume fraction (MVF) which can be calculated by Hernandez-Lagoudas model as expressed in Appendix B.

3. Motion equations

The potential energy of the MRF with NFRP layers and SMA are

$$U=\int_x\left(N_x\frac{\partial u_i}{\partial x}-M_x\frac{\partial^2 w_i}{\partial x^{\ 2}}+P_x\frac{\partial\psi_i}{\partial x}+Q_x\psi_i\right)dx, \quad (11)$$

where i=1-7. The plane forces and moments as well as moment of inertias are:

$$\begin{aligned}(N_x,M_x,P_x)&=\int_{-\frac{h_c}{2}-h_f}^{-\frac{h_c}{2}}\sigma_{xx}^n(1,z,f)\,dz\\&+\int_{-\frac{h_c}{2}}^{\frac{h_c}{2}}\sigma_{xx}^c(1,z,f)dz+\int_{\frac{h_c}{2}}^{\frac{h_c}{2}+h_f}\sigma_{xx}^n(1,z,f)dz\\&+\int_{-h_c/2}^{h_c/2}\sigma_{xx}^s(1,z,f)dz,\end{aligned} \quad (12)$$

$$\begin{aligned}Q_x&=\int_{-\frac{h_c}{2}-h_f}^{-\frac{h_c}{2}}\sigma_{xz}^n\frac{\partial f}{\partial z}dz+\int_{-\frac{h_c}{2}}^{\frac{h_c}{2}}\sigma_{xz}^c\frac{\partial f}{\partial z}dz\\&+\int_{h_c/2}^{h_c/2+h_f}\sigma_{xz}^n\frac{\partial f}{\partial z}dz+\int_{-h_c/2}^{h_c/2}\sigma_{xz}^s\frac{\partial f}{\partial z}dz,\end{aligned} \quad (13)$$

The kinetic energy of the MRF with NFRP layers and SMA are

$$K=\int\begin{bmatrix}I_0\left(\left(\frac{\partial u_i}{\partial t}\right)^2+\left(\frac{\partial w_i}{\partial t}\right)^2\right)-I_1\left(\frac{\partial u_i}{\partial t}\frac{\partial^2 w_i}{\partial t\partial x}+\frac{\partial u_i}{\partial t}\frac{\partial^2 w_i}{\partial t\partial x}\right)\\ +I_2\frac{\partial^2 w_i}{\partial x\partial t}\frac{\partial^2 w_i}{\partial x\partial t}+I_3\left(\frac{\partial u}{\partial t}\frac{\partial\psi_i}{\partial t}+\frac{\partial u}{\partial t}\frac{\partial\psi_i}{\partial t}\right)\\ -I_4\left(\frac{\partial^2 w_i}{\partial t\partial x}\frac{\partial\psi_i}{\partial t}+\frac{\partial^2 w_i}{\partial t\partial x}\frac{\partial\psi_i}{\partial t}\right)+I_5\frac{\partial\psi_i}{\partial t}\frac{\partial\psi_i}{\partial t}\end{bmatrix}dx \quad (14)$$

where the moments of inertia are

$$\begin{aligned}(I_0,I_1,I_2,I_3,I_4,I_5)&=\int_{-\frac{h_c}{2}-h_f}^{-\frac{h_c}{2}}\rho^n(1,z,z^2,f,zf,f^2)\,dz\\&+\int_{-\frac{h_c}{2}}^{\frac{h_c}{2}}\rho^c(1,z,z^2,f,zf,f^2)\,dz\\&+\int_{\frac{h_c}{2}}^{\frac{h_c}{2}+h_f}\rho^n(1,z,z^2,f,zf,f^2)\,dz\\&++\int_{-h_c/2}^{h_c/2}\rho^s(1,z,z^2,f,zf,f^2)\,dz,\end{aligned} \quad (15)$$

where ρ^n, ρ^c and ρ^s are density of NFRP, concrete and SMA, respectively. The external work due to the earthquake load is

$$W=\int(\underbrace{ma(t)}_{F_{Seismic}})u dA, \quad (16)$$

in which m and $a(t)$ are the structure mass and earthquake acceleration, respectively. Hamilton's principle is utilized as:

$$\int_0^t(\delta U-\delta K-\delta W)dt=0, \quad (17)$$

Substituting Eqs. (12), (14) and (16) into Eq. (18) yields the following coupled motion equations for horizontal beams (i.e. beams number 3,4,5):

$$\delta u:\frac{\partial N_x}{\partial x}=I_0\frac{\partial^2 u}{\partial t^2}. \quad (18)$$

$$\delta w:\frac{\partial^2 M_x}{\partial x^{\ 2}}=I_0\frac{\partial^2 w}{\partial t^2}+\frac{24I_2}{\pi^3}\frac{\partial^2\psi}{\partial x\partial t}-I_2\frac{\partial^4 w}{\partial x^{\ 2}\partial t^2}+F_{Seismic}, \quad (19)$$

$$\delta\psi:\frac{\partial P_x}{\partial x}-Q_x=\frac{6I_2}{\pi^2}\frac{\partial^2\psi}{\partial t^2}-\frac{24I_2}{\pi^3}\frac{\partial^2 w}{\partial x\partial t}. \quad (20)$$

The above motion equations for vertical beams (i.e., beams number 1,2,6,7) are:

$$\delta u:\frac{\partial N_x}{\partial x}=I_0\frac{\partial^2 u}{\partial t^2}. \quad (21)$$

$$\begin{aligned}\delta w:\frac{\partial^2 M_x}{\partial x^{\ 2}}&=I_0\frac{\partial^2 w}{\partial t^2}+\frac{24I_2}{\pi^3}\frac{\partial^2\psi}{\partial x\partial t}-I_2\frac{\partial^4 w}{\partial x^{\ 2}\partial t^2}\\&-\rho gA\frac{\partial}{\partial x}\left[(L-x)\frac{\partial w}{\partial x}\right]+F_{Seismic},\end{aligned} \quad (22)$$

$$\delta\psi:\frac{\partial P_x}{\partial x}-Q_x=\frac{6I_2}{\pi^2}\frac{\partial^2\psi}{\partial t^2}-\frac{24I_2}{\pi^3}\frac{\partial^2 w}{\partial x\partial t}. \quad (23)$$

The general boundary conditions assumed in this paper are

$$\begin{aligned}w_3=u_3=\frac{\partial w_3}{\partial x_3}=0@x_3=0\\ w_2=u_2=\frac{\partial w_2}{\partial x_2}=0@x_2=0\end{aligned} \quad (24)$$

The continuity boundary conditions between the beam and columns of the concrete frame are about the equality of axial and transverse deflection, axial force and moments. For example, between columns 1 and 2, we have:

$$\begin{cases} w_1 = w_2 \\ u_1 = u_2 \\ M_{x1} = M_{x2} \\ N_{x1} = N_{x2} \end{cases} @x_1 = L_1 \tag{25}$$

In fact, we have 7 beams and hence, 7*3=21 motion equations and these equations can be coupled by continuity boundary conditions.

4. Numerical method

4.1 DC method

The basic relation of the DC method which shows an algebric relation can be given as (Al-Furjan *et al*. 2021, Motezaker *et al*. 2021a, b, 2022a, b, Kolahchi *et al*. 2017, Keshtegar *et al*. 2020)

$$\Re f(x,y)_i \approx \sum_{j=1}^{N} C_{ij} f(x_j, y_j), \tag{26}$$

where $\Re$ is a calculus operator, $f(x,y)$ is a function, C_{ij} and N are the cubature weighting coefficients and grid points number, respectively. The calculation of the weighting coefficients may be presented as

$$\Re\{x^{\nu-\mu}y^{\mu}\}_i = \sum_{j=1}^{N} C_{ij} f(x_j^{\nu-\mu} y_j^{\mu}), \mu = 0,1,2,\ldots,\nu, \nu = 0,1,2,\ldots,N-1, i = 1,2,\ldots,N. \tag{27}$$

The above relation in matrix form is

$$\left[x_j^{\nu-\mu} y_j^{\mu}\right] \begin{bmatrix} C_{i1} \\ C_{i2} \\ . \\ . \\ C_{in} \end{bmatrix} = [\Re\{x^{\nu-\mu}y^{\mu}\}_i]. \tag{28}$$

By solving Eq. (28), the cubature weighting coefficients can be calculated and finally, the motion equations in matrix form based on DC method may be given as

$$\left([K]\begin{Bmatrix}\{d_b\}\\ \{d_d\}\end{Bmatrix} + [C]\begin{Bmatrix}\{\dot{d}_b\}\\ \{\dot{d}_d\}\end{Bmatrix} + [M]\begin{Bmatrix}\{\ddot{d}_b\}\\ \{\ddot{d}_d\}\end{Bmatrix}\right) = \begin{Bmatrix}\{0\}\\ -Ma(t)\end{Bmatrix}, \tag{29}$$

where $[M]$, $[C]$ and $[K]$ are respectively, the mass matrix, damp matrix and stiffness matrix. In addition, $\{d_b\}$ and $\{d_a\}$ are the boundary and domain points, respectively.

4.2 Newmark scheme

Newmark's numerical method is applied for solution of the problem under the earthquake load. The basic relation of this method is

$$K^*(d_{i+1}) = Q_{i+1}, \tag{30}$$

where $K^*(d_{i+1})$ and $Q_{i+1}$are the effective matrix and force, respectively which are

$$K^*(d_{i+1}) = K_L + K_{NL}(d_{i+1}) + \alpha_0 M + \alpha_1 C, \tag{31}$$

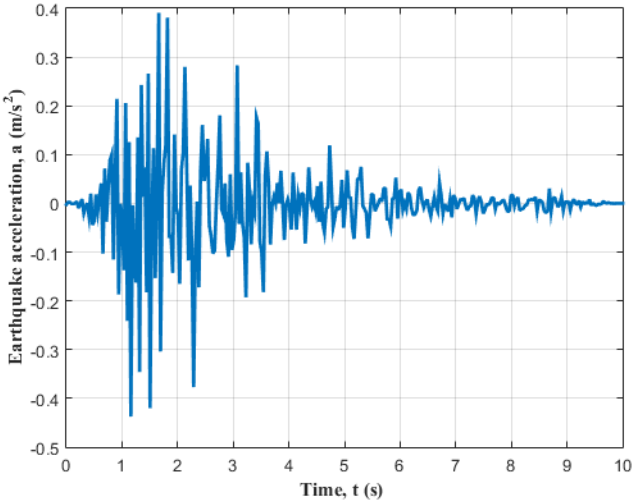

Fig. 2 Acceleration of the Lom Prieta earthquake

$$Q_{i+1}^* = Q_{i+1} + M(\alpha_0 d_i + \alpha_2 \dot{d}_i + \alpha_3 \ddot{d}_i) + C(\alpha_1 d_i + \alpha_4 \dot{d}_i + \alpha_5 \ddot{d}_i), \tag{32}$$

in which

$$\alpha_0 = \frac{1}{\chi \Delta t^2}, \alpha_1 = \frac{\gamma}{\chi \Delta t}, \alpha_2 = \frac{1}{\chi \Delta t}, \alpha_3 = \frac{1}{2\chi} - 1, \alpha_4 = \frac{\gamma}{\chi} - 1, \alpha_5 = \frac{\Delta t}{2}\left(\frac{\gamma}{\chi} - 2\right), \alpha_6 = \Delta t(1-\gamma), \alpha_7 = \Delta t \gamma, \tag{33}$$

where $\gamma = 0.5$ and $\chi = 0.25$. In addition, the modified acceleration and velocity of the structure may be given as

$$\ddot{d}_{i+1} = \alpha_0(d_{i+1} - d_i) - \alpha_2 \dot{d}_i - \alpha_3 \ddot{d}_i, \tag{34}$$

$$\dot{d}_{i+1} = \dot{d}_i + \alpha_6 \ddot{d}_i + \alpha_7 \ddot{d}_{i+1}, \tag{35}$$

5. Results and discussion

For parametric study, a concrete frame with length of $L_1 = L_7 = 6m$, $L_4 = 5m$, $L_{SMA} = 0.5m$, concrete thickness of $h_c = 30cm$ and NFRP thickness of $h_f = 1cm$is assumed. The Young's modulus of concrete, NFRP and SMA are assumed as $E_{Concrete} = 20GPa$, $E_{NFRP} = 40GPa$ and $E_{SMA}|_A = 32.5GPa, E_{SMA}|_M = 23GPa$, respectively (Brinson, 1993). The Lom Prieta region is assumed for earthquake acceleration (Fig. 2) with Magnitude of 6.9.

5.1 Validation of results

In order to validate the results of this paper, the drift ratio of a concrete frame with steel bars and Superelastic shape memory alloy (SE-SMA) is studied based on the material properties of Abraik (2020). As can be seen from Table 1, the drift ratio of Abraik (2020) and present work are the same which show the accuracy of present mathematical model and numerical solution.

Table 1 Validation of this work with Ref (Abreik 2020)

Time	Steel-reinforced frame		SE-SMA-reinforced frame	
	Ref. (2020)	Present	Ref. (2020)	Present
0.50 s	1.2	1.22	0.95	1.24
1.75 s	2.5	2.57	6.1	6.15
2.25 s	3.8	3.79	7.5	7.51
2.75 s	4.4	4.45	9.5	9.52

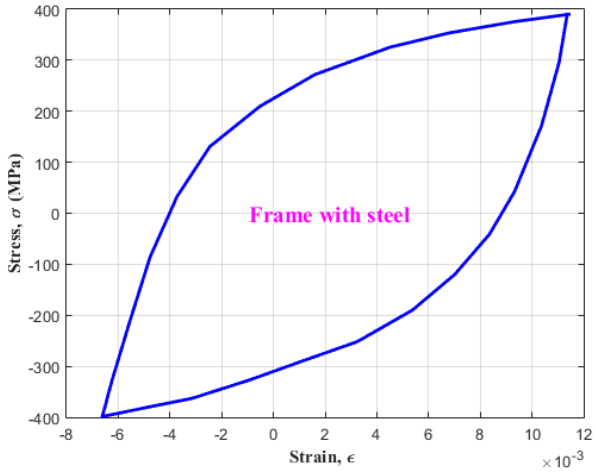

Fig. 3 The hysteresis loops of the concrete frame with steel bars

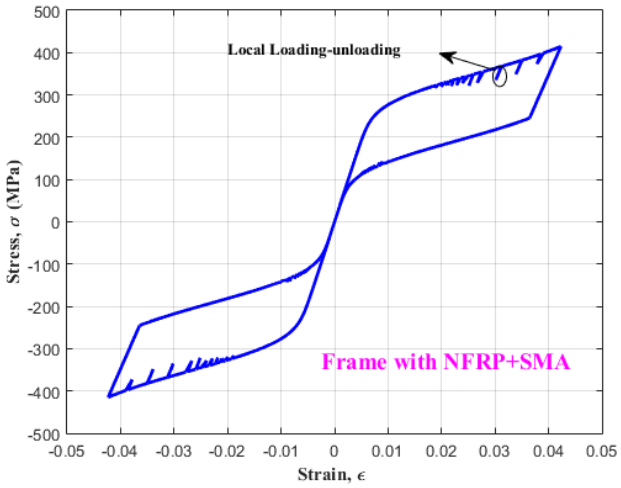

Fig. 4 The hysteresis loops of the concrete frame with NFRP layers and SMA

5.2 PGA and drift ratio

Figs. 3 and 4, respectively indicates the hysteresis loops of concrete frame with steel bars and concrete frame with SMA-NFRP. Maximum strain obtained by the concrete frame with steel bars is 1.19%. Steel material response indicates a residual strain due to the damage of MRF. Based on Fig. 4, it can be found that the maximum strain is 4.1% which is enhanced about 71%. In addition, the residual drift ration is zero in concrete frame with SMA-NFRP.

Figs. 5-7 illustrate the drift ratio time history of the structure with MFR-2%, respectively, for concrete frame

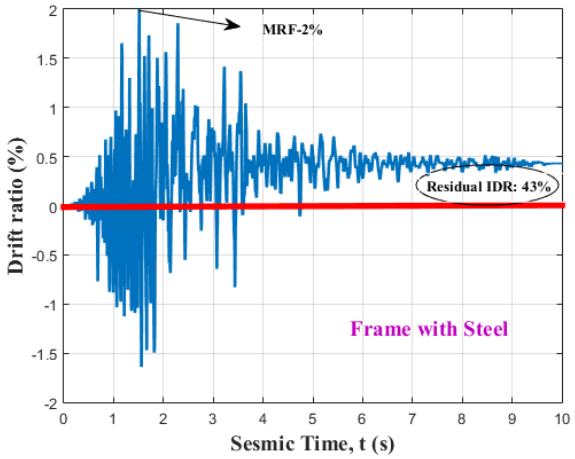

Fig. 5 The drift ratio time history of the concrete frame with steel bars

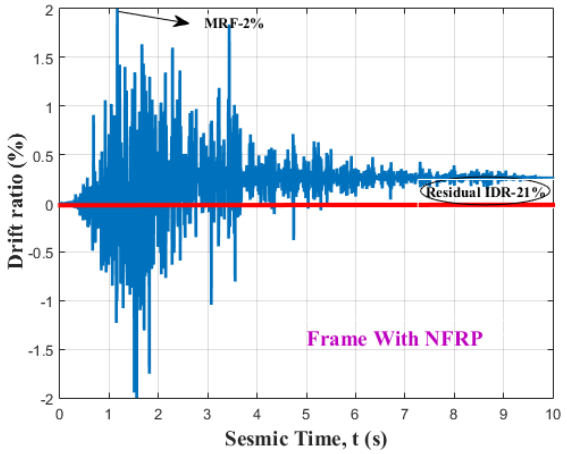

Fig. 6 The drift ratio time history of the concrete frame with NFRP layers

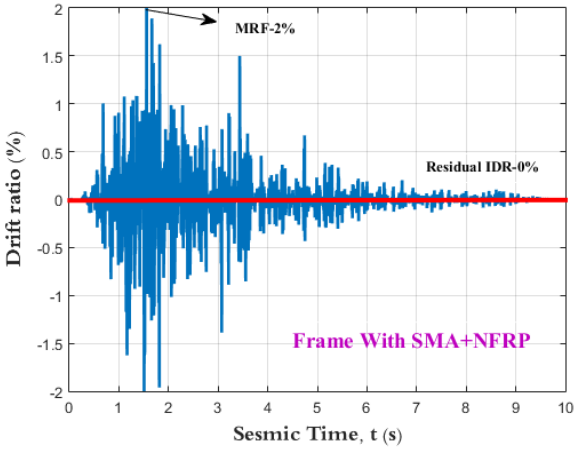

Fig. 7 The drift ratio time history of the concrete frame with NFRP layers and SMA

with steel bars, with NFRP and with SMA-NFRP. The Lom Prieta earthquake is necessary to be scaled to PGA of 2.18 g, 1.62 g and 1.16 g to cause 2% drift ratio for steel, NFRP and SMA–NFRP reinforced concrete frames, respectively. This is physically reasonable, since the steel bars has higher inherent stiffness with respect to NFRP and SMA-NFRP

Table 2 The effect of column length and thickness on the PGA and residual drift ratio in the frame for MRF-2%

Type of Frame	L_1 (m)	PGA			Residual drift ratio (%)		
		h_c=30 cm	h_c=40 cm	h_c=50 cm	h_c=30 cm	h_c=40 cm	h_c=50 cm
With Steel	5	2.42g	2.61g	2.88g	40.23	42.44	44.17
	6	2.18g	2.36g	2.55g	43.19	45.09	48.38
	7	1.97g	2.15g	2.33g	46.03	48.22	49.98
With NFRP	5	2.02	2.31	2.62	18.17	21.11	24.48
	6	1.62	1.93	2.23	21.18	24.42	27.09
	7	1.30	1.67	1.93	24.66	27.09	30.17
With NFRP+SMA	5	1.55	1.90	2.25	0	0	0
	6	1.16	1.55	1.83	0	0	0
	7	0.77	1.12	1.48	0	0	0

Table 3 The effect of volume percent and agglomeration of nanofibers on PGA and residual drift ratio in the frame for MRF-2%

Type of Frame	Aglomeration	PGA			Residual drift ratio (%)		
		C_r=0	C_r=1%	C_r=2%	C_r=0	C_r=1%	C_r=2%
With Steel	$\xi = 1.0$	2.18g	---	---	43.19	---	---
	$\xi = 0.8$	---	---	---	---	---	---
	$\xi = 0.5$	---	---	---	---	---	---
With NFRP	$\xi = 1.0$	1.04	1.84	2.11	30.27	17.82	10.87
	$\xi = 0.8$	1.04	1.62	1.91	30.27	21.18	15.44
	$\xi = 0.5$	1.04	1.42	1.77	30.27	25.41	21.09
With NFRP+SMA	$\xi = 1.0$	0.55	1.44	1.67	0	0	0
	$\xi = 0.8$	0.55	1.16	1.43	0	0	0
	$\xi = 0.5$	0.55	0.89	1.27	0	0	0

reinforced frames. In comparison of NFRP and SMA-NFRP reinforced frames, the PGA for reach to MRF-2% of NFRP reinforced frame is higher than SMA-NFRP reinforced frame since the in second case, existence of SMA increases the ductility. It is worth to mention that residual drift ratio is 43% for steel reinforced concrete frame while this is 21% and zero for NFRP and SMA-NFRP reinforced concrete frames, respectively. From the physical view, since the ductility of NFRP reinforced concrete frames is higher than steel reinforced concrete frames, hence its residual drift ratio is lower. In addition, due to re-centering capability of SMA hinges, there is not residual drift ratio and permanent damage in the concrete frame. This figure (i.e., Fig. 8) shows the importance of SMA in concrete structure under the earthquake load.

Tables 2-4 shows the effect of various parameters of the PGA and residual drift ratio for MRF-2%. In Table 2, the effects of column length and thickness of concrete are presented on the PGA and residual drift ratio. As can be seen, with increasing the thickness of the frame and reducing the length of column number 1, the PGA is increased since the stiffness of the structure is improved. In addition, the PGA for the steel reinforced concrete frame is higher than NFRP and SMA-NFRP reinforced concrete frame. It is also worth to mention that the effect of column length and thickness on the PGA is higher in SMA-NFRP reinforced concrete frame with respect to steel reinforced concrete frame due to more ductility in the structure. For the influence of parameters on the residual drift ratio, it is found that in steel and NFRP reinforced concrete frame, it is enhanced with increasing the thickness and column length. Noted that the residual drift ratio is zero for the case of SMA-NFRP reinforced concrete frame due to re-centering capability of SMA hinges.

The effects of volume percent and agglomeration of nanofibers on the PGA and residual drift ratio are demonstrated in Table 3 for MRF-2%. It is vivid that for NFRP reinforced concrete frame, with increasing the volume percent of nanofibers, the PGA for MRF-2% is increased and the residual drift ratio is decreased. It is due to this fact that with enhancing the volume percent of nanofibers, the bending rigidity and energy dissipation of the structure are improved. Furthermore, with increasing the agglomeration of nanofibers, the PGA for MRF-2% is decreased while the residual drift ratio is increased. It is true from the physical view, since the agglomeration of nano-fibers reduced the stiffness and stability of the structure. The most important result of this figure is that in the case of NFRP reinforced concrete frame with nanofibers volume percent of 2% without agglomeration, the PGA is approximately equal to steel reinforced concrete frame. In addition, in this case, the residual drift ratio is in minimum

Table 4 The effect of MRF and volume percent of nanofibers on PGA and residual drift ratio of the frame for MRF-2%

Type of Frame	MRF	PGA			Residual drift ratio (%)		
		C_r=0	C_r=1%	C_r=2%	C_r=0	C_r=1%	C_r=2%
With Steel	2%	2.18g	---	---	43.19	---	---
	3%	2.33g	---	---	56.12	---	---
	4%	3.63g	---	---	62.17	---	---
With NFRP	2%	1.04	1.62	1.91	30.27	21.18	15.44
	3%	1.23	1.88	2.12	35.23	25.38	19.87
	4%	1.45	2.02	2.37	39.44	30.01	24.44
With NFRP+SMA	2%	0.55	1.16	1.43	0	0	0
	3%	0.88	1.47	1.61	0	0	0
	4%	1.17	1.75	1.86	0	0	0

state with respect to other cases. Hence, the NFRP layers can be a suitable alternative for steel in concrete structures.

Table 4 illustrates the effect of MRF and volume percent of nanofibers on the PGA and drift ratio for MRF-2%. It is observed that with enhancing the MRF, the PGA and residual drift ratio are increased since the dynamic deflection in this case is higher with respect to MRF-2% and 3%.

6. Conclusions

In MFR, the main ductility occurs in the end areas of the beams by creating the plastic joints. In order to reduces the life threatening risks and improve the seismic response of concrete frames, the NFRP layers and SMA materials were used. The TASDT was applied for mathematical modelling of the structure and the continuity boundary conditions were used for coupling of the motion equations. The nanofibers in NFRP layer were modelled by Mori-Tanaka theory while for phase transformation in SMA beams, the Hernandez-Lagoudas theory was utilized. The combination of DC-Newmark methods was used in order to obtain the PGA for MRF-2% and residual drift ratio. The important results of this article were:

• Maximum strain obtained by the concrete frame with steel bars was 1.19% while it was 4.1% for SMA-NFRP reinforced frame which was enhanced about 71%.

• The Lom Prieta earthquake was necessary to be scaled to PGA of 2.18 g, 1.62 g and 1.16 g to cause 2% drift ratio for steel, NFRP and SMA–NFRP reinforced concrete frames, respectively.

• It was worth to mention that residual drift ratio was 43% for steel reinforced concrete frame while this was 21% and zero for NFRP and SMA-NFRP reinforced concrete frames, respectively.

• Due to re-centering capability of SMA hinges, there was not residual drift ratio and permanent damage in the concrete frame.

• It was found that the effect of column length and thickness on the PGA was higher in SMA-NFRP reinforced concrete frame with respect to steel reinforced concrete frame.

• It was vivid that for NFRP reinforced concrete frame, with increasing the volume percent of nanofibers, the PGA for MFR-2% was increased and the residual drift ratio was decreased.

• The most important result of this paper was that in the case of NFRP reinforced concrete frame with nanofibers volume percent of 2% without agglomeration, the PGA for MFR-2% was approximately equal to steel reinforced concrete frame.

References

Al-Furjan, M.S.H., Farrokhian, A., Mahmoud, S.R. and Kolahchi, R. (2021), "Dynamic deflection and contact force histories of graphene platelets reinforced conical shell integrated with magnetostrictive layers subjected to low-velocity impact", *Thin-Wall. Struct.*, **163**, 107706. https://doi.org/10.1016/j.tws.2021.107706.

Al-Furjan, M.S.H., Shan, L., Shen, X., Kolahchi, R. and Rajak, D.K. (2022a), "Combination of FEM-DQM for nonlinear mechanics of porous GPL-reinforced sandwich nanoplates based on various theories", *Thin Wall. Struct.*, **178**, 109495, https://doi.org/10.1016/j.tws.2022.109495.

Al-Furjan, M.S.H., Yin, C., Shen, X., Kolahchi, R., Zarei, M.Sh. and Hajmohammad, M.H. (2022b), "Energy absorption and vibration of smart auxetic FG porous curved conical panels resting on the frictional viscoelastic torsional substrate", *Mech. Syst. Sign. Proc.*, **178**, 109269, https://doi.org/10.1016/j.ymssp.2022.109269.

Abreik, E. (2020), "Seismic performance of shape memory alloy reinforced concrete moment frames under sequential seismic hazard", *Structures*, **26**, 311-326. https://doi.org/10.1016/j.istruc.2020.04.025.

Abou-Elfath, H. (2018), "Ductility characteristics of concrete frames reinforced with superelastic shape memory alloys", *Alexand. Eng. J.*, **57**(4), 4121-4132. https://doi.org/10.1016/j.aej.2018.10.013

Alam, M.S. and Moni, M. (2012), "Tesfamariam S. Seismic overstrength and ductility of concrete buildings reinforced with superelastic shape memory alloy rebar", *Eng. Struct.* **34**, 8-20. https://doi.org/10.1016/j.engstruct.2011.08.030.

Al-Osta, M.A., Saidi, H., Tounsi, A., Al-Dulaijan, S.U., Al-Zahrani, M.M., Sharif, A and Tounsi, A. (2021), "Influence of porosity on the hygro-thermo-mechanical bending response of an AFG ceramic-metal plates using an integral plate model",

Smart Struct. Syst., **28**(4), 499-513. https://doi.org/10.12989/sss.2021.28.4.499.

Bekkaye, T.H.L., Fahsi, B., Bousahla, A.A., Bourada, F., Tounsi, A., Benrahou, K.H. and Al-Zahrani, M.M. (2020), "Porosity-dependent mechanical behaviors of FG plate using refined trigonometric shear deformation theory", *Comput. Concr.*, **26**(5), 439-450. https://doi.org/10.12989/CAC.2020.26.5.439.

Blazy, J. and Blazy, R. (2021), "Polypropylene fiber reinforced concrete and its application in creating architectural forms of public spaces", *Case Stud. Constr. Mater.*, **14**, e00549. https://doi.org/10.1016/j.cscm.2021.e00549.

Brinson, L.C. (1993), "One-dimensional constitutive model of shape memory alloys: thermomechanical derivation with non-constant material functions", *J. Intell. Mater. Syst. Struct.*, **4**(2), 229-242, https://doi.org/10.1177/1045389X9300400213.

Ding, H., Kaup, A., Wang, J.T., Lu, L.Q. and Altay, A. (2021), "Real-time hybrid simulation framework for the investigation of soil-structure interaction effects on the vibration control performance of shape memory alloys", *Eng. Struct.*, **243**, 112621. https://doi.org/10.1016/j.engstruct.2021.112621.

Elfeki, M.A. and Youssef, M.A. (2017), "Shape memory alloy reinforced concrete frames vulnerable to strong vertical excitations", *J. Build. Eng.*, **13**, 272-290. https://doi.org/10.1016/j.jobe.2017.08.011.

Gur, S., Frantziskonis, G.N. and Mishra, S.K. (2017), "Thermally modulated shape memory alloy friction pendulum (tmSMA-FP) for substantial near-fault earthquake structure protection", *Struct. Cont. Heal. Monitor.*, **24**, 88-101, https://doi.org/10.1002/stc.2021.

Hajlaoui, A., Chebbi, E. and Dammak, F. (2019), "Buckling analysis of carbon nanotube reinforced FG shells using an efficient solid-shell element based on modified FSDT", *Thin-Wall. Struct.*, **144**, 106254. https://doi.org/10.1016/j.tws.2019.106254.

Hajlaoui, A., Chebbi, E., Wali, M. and Dammak, F. (2020a), "Geometrically nonlinear analysis of FGM shells using solid-shell element with parabolic shear strain distribution", *Int. J. Mech. Mat. Des.*, **16**, 351-366. https://doi.org/10.1007/s10999-019-09465-x.

Hajlaoui, A., Chebbi, E., Wali, M. and Dammak, F. (2020b), "Static analysis of carbon nanotube-reinforced FG shells using an efficient solid-shell element with parabolic transverse shear strain", *Eng. Comput.*, **37**(3), 823-849. https://doi.org/10.1108/EC-02-2019-0075.

Hajmohammad, M.H., Maleki, M. and Kolahchi, R. (2018), "Seismic response of underwater concrete pipes conveying fluid covered with nano-fiber reinforced polymer layer", *Soil Dyn. Earthq. Eng.*, **110**, 18-27. https://doi.org/10.1016/j.soildyn.2018.04.002.

Huang, H. and Chang, W.S. (2017), "Seismic resilience timber connection—adoption of shape memory alloy tubes as dowels", *Struct. Cont. Heal. Monitor.*, **24**, 56-72, https://doi.org/10.1002/stc.1980.

Hosseini, A., Michels, J., Izadi, M. and Ghafoori, E. (2019), "A comparative study between Fe-SMA and CFRP reinforcements for prestressed strengthening of metallic structures", *Constr. Build. Mater.*, **226**, 976-992. https://doi.org/10.1016/j.conbuildmat.2019.07.169.

Jassas, M.R., Bidgoli, M.R. and Kolahchi, R. (2019), "Forced vibration analysis of concrete slabs reinforced by agglomerated SiO2 nanofibers based on numerical methods", *Constr. Build. Mater.*, **211**, 796-806, https://doi.org/10.1016/j.conbuildmat.2019.03.263.

Jeon, E.B., Ahn, S.K., Lee, I.G., Koh, H.I., Park, J. and Kim, H.S. (2015), "Investigation of mechanical/dynamic properties of carbon fiber reinforced polymer concrete for low noise railway slab", *Compos. Struct.*, **134**, 27-35. https://doi.org/10.1016/j.compstruct.2015.08.082.

Karimipour, A. and Edalati, M. (2020), "Shear and flexural performance of low, normal and high-strength concrete beams reinforced with longitudinal SMA, GFRP and steel rebars", *Eng. Struct.*, **221**, 111086. https://doi.org/10.1016/j.engstruct.2020.111086.

Keshtegar, B., Tabatabaei, J., Kolahchi, R. and Trung, N.T. (2020), "Dynamic stress response in the nanocomposite concrete pipes with internal fluid under the ground motion load", *Adv. Concr. Constr.*, **9**(3), 327-335, https://doi.org/10.12989/acc.2020.9.3.327.

Kolahchi, R. (2017), "A comparative study on the bending, vibration and buckling of viscoelastic sandwich nano-plates based on different nonlocal theories using DC, HDQ and DQ methods", *Aerosp. Sci. Technol.*, **66**, 235-248, https://doi.org/10.1016/j.ast.2017.03.016.

Kumar, Y., Gupta, A. and Tounsi, A. (2021), "Size-dependent vibration response of porous graded nanostructure with FEM and nonlocal continuum model", *Adv. Nano Res.*,**11**(1), 1-17. https://doi.org/10.12989/anr.2021.11.1.001.

Lagoudas, D.C., Hartl, D., Chemisky, Y., Machado, L. and Popov, P. (2012), "Constitutive model for the numerical analysis of phase transformation in polycrystalline shape memory alloys", *Int. J. Plas.*, **32**, 155-183, https://doi.org/10.1016/j.ijplas.2011.10.009.

Lee, C.S., Choi, E. and Jeon, J.S. (2022), "Estimating the plastic hinge length of rectangular concrete columns reinforced with NiTi superelastic shape memory alloys", *Eng. Struct.*, **252**, 113641. https://doi.org/10.1016/j.engstruct.2021.113641.

Lobo, P.S., Almeida, J. and Guerreiro, L. (2017), "Recentring and control of peak displacements of a RC frame using damping devices", *Soil Dynam. Earthq. Eng.*, **94**, 66-74. https://doi.org/10.1016/j.soildyn.2017.01.003.

Moni, M. (2011), *Performance of Shape Memory Alloy Reinforced Concrete Frames Under Extreme Loads*, University of British Columbia. England.

Mahjoobi, M. and Rabani Bidgoli, M. (2019), "Dynamic deflection analysis induced by blast load in viscoelastic sandwich plates with nanocomposite facesheets", *J. Sandw. Struct. Mater.*, **23**(4), 1118-1140. https://doi.org/10.1177/1099636219853189.

Mahjoobi, M., Rabani Bidgoli, M and Mazaheri, M. (2021a), "Dynamic analysis of quadrilateral concrete foundation integrated with NFRP layers based on numerical method", *Adv. nano Res.*, **11**(5), 537-546. https://doi.org/10.12989/anr.2021.11.5.537.

Motezaker, M., Kolahchi, R., Rajak, D.K. and Mahmoud, S.R. (2021b), "Influences of fiber reinforced polymer layer on the dynamic deflection of concrete pipes containing nanoparticle subjected to earthquake load", *Polym. Compos.*, **42**, 4073-4081, https://doi.org/10.1002/pc.26118.

Muntasir Billah, A.H.M. and Shahria Alam, M. (2016), "Plastic hinge length of shape memory alloy (SMA) reinforced concrete bridge pier", *Eng. Struct.*, **117**, 321-331. https://doi.org/10.1016/j.engstruct.2016.02.050.

Navarro-Gómez, A. and Bonet, J.L. (2019), "Improving the seismic behaviour of reinforced concrete moment resisting frames by means of SMA bars and ultra-high performance concrete", *Eng. Struct.*, **197**, 109409. https://doi.org/10.1016/j.engstruct.2019.109409.

Nunes, P and Silva Lobo P. (2019), "Influence of the SMA constitutive model on the longitudinal seismic response of RC bridges", *Procedia Struct. Integrity*, **17**, 624-631. https://doi.org/10.1016/j.prostr.2019.08.084.

Oudah, F. and El-Hacha, R. (2018), "Innovative self-centering concrete beam-column connection reinforced using shape memory alloy", *ACI Struct. J.*, **115**(3). 22-36,

https://doi.org/10.14359/51702132.
Ouyang, L.J., Gao, W.Y., Zhen, B. and Lu, Z.D. (2017), "Seismic retrofit of square reinforced concrete columns using basalt and carbon fiber-reinforced polymer sheets: A comparative study", *Compos. Struct.*, **162**, 294-307, https://doi.org/10.1016/j.compstruct.2016.12.016.
Pareek, S., Suzuki, Y., Youssef, M.A. and Meshaly, M. (2018), "Plastic hinge relocation in reinforced concrete beams using Cu-Al-Mn SMA bars", *Eng. Struct.*, **175**, 765-775. https://doi.org/10.1016/j.engstruct.2018.08.072.
Rojob, H. and El-Hacha, R. (2017), "Self-prestressing using iron-based shape memory alloy for flexural strengthening of reinforced concrete beams", *ACI Struct. J.*, **114**(2), 523-532. https://doi.org/10.14359/51689455.
Safari Bilouei, B., Kolahchi, R. and Rabani Bidgoli, M. (2016), "Buckling of concrete columns retrofitted with Nano-Fiber Reinforced Polymer (NFRP)", *Comput. Concr.*, **18**(5), 1053-1063. https://doi.org/10.12989/cac.2016.18.5.1053.
Siddiquee, K.N., Muntasir Billah, A.H.M. and Issa, A. (2021), "Seismic collapse safety and response modification factor of concrete frame buildings reinforced with superelastic shape memory alloy (SMA) rebar", *J. Build. Eng.*, **42**, 102468. https://doi.org/10.1016/j.jobe.2021.102468.
Shariati Rad, S. and Rabani Bidgoli, M. (2017), "Earthquake analysis of NFRP-reinforced-concrete beams using hyperbolic shear deformation theory", *Earthq. Struct.*, **13**(3), 241-253. https://doi.org/10.12989/eas.2017.13.3.241.
Simsek, M. and Reddy, J.N. (2013), "Bending and vibration of functionally graded microbeams using a new higher order beam theory and the modified couple stress theory", *Int. J. Eng. Sci.*, **64**, 37-53. https://doi.org/10.1016/j.ijengsci.2012.12.002.
Tahir, S.I., Chick, A., Tounsi, A., Al-Osta, M.A., Al-Dulaijan, S.U. and Al-Zahrani, M.M. (2021), "Wave propagation analysis of a ceramic-metal functionally graded sandwich plate with different porosity distributions in a hygro-thermal environment", *Compos. Struct.*, **269**, 114030. https://doi.org/10.1016/j.compstruct.2021.114030.
Yuan, C., Chen, W., Pham, T.M., Hao, H., Cui, J. and Shi, Y. (2020), "Dynamic interfacial bond behaviour between basalt fiber reinforced polymer sheets and concrete", *Int. J. Solids Struct.*, **202**, 587-604. https://doi.org/10.1016/j.ijsolstr.2020.07.007.
Zafar, A. and Andrawes, B. (2015), "Seismic behavior of SMA–FRP reinforced concrete frames under sequential seismic hazard", *Eng. Struct.*, **98**, 163-173. https://doi.org/10.1016/j.engstruct.2015.03.045.
Zamani, A. and Rabani Bidgoli, M. (2017), "Vibration analysis of concrete foundations retrofit with NFRP layer resting on soil medium using sinusoidal shear deformation theory", *Soil Dyn. Earthquake Eng.*, **103**, 141-150. https://doi.org/10.1016/j.soildyn.2017.09.018.

AT

Appendix A

$$K = K_{out}\left[1+\frac{\xi\left(\frac{K_{in}}{K_{out}}-1\right)}{1+\alpha(1-\xi)\left(\frac{K_{in}}{K_{out}}-1\right)}\right], \tag{A1}$$

$$G = G_{out}\left[1+\frac{\xi\left(\frac{G_{in}}{G_{out}}-1\right)}{1+\beta(1-\xi)\left(\frac{G_{in}}{G_{out}}-1\right)}\right], \tag{A2}$$

where

$$K_{in} = K_m + \frac{(\delta_r - 3K_m\chi_r)C_r\zeta}{3(\xi - C_r\zeta + C_r\zeta\chi_r)}, \tag{A3}$$

$$K_{out} = K_m + \frac{C_r(\delta_r - 3K_m\chi_r)(1-\zeta)}{3[1-\xi-C_r(1-\zeta)+C_r\chi_r(1-\zeta)]}, \tag{A4}$$

$$G_{in} = G_m + \frac{(\eta_r - 3G_m\beta_r)C_r\zeta}{2(\xi - C_r\zeta + C_r\zeta\beta_r)}, \tag{A5}$$

$$G_{out} = G_m + \frac{C_r(\eta_r - 3G_m\beta_r)(1-\zeta)}{2[1-\xi-C_r(1-\zeta)+C_r\beta_r(1-\zeta)]}, \tag{A6}$$

where $\chi_r, \beta_r, \delta_r, \eta_r$ may be calculated as

$$\chi_r = \frac{3(K_m+G_m)+k_r-l_r}{3(k_r+G_m)}, \tag{A7}$$

$$\begin{aligned}\beta_r &= \frac{1}{5}\left\{\frac{4G_m+2k_r+l_r}{3(k_r+G_m)}+\frac{4G_m}{(p_r+G_m)}\right.\\ &\left.+\frac{2[G_m(3K_m+G_m)+G_m(3K_m+7G_m)]}{G_m(3K_m+G_m)+m_r(3K_m+7G_m)}\right\},\end{aligned} \tag{A8}$$

$$\delta_r = \frac{1}{3}\left[n_r+2l_r+\frac{(2k_r-l_r)(3K_m+2G_m-l_r)}{k_r+G_m}\right], \tag{A9}$$

$$\eta_r = \frac{1}{5}\left[\begin{array}{c}\frac{2}{3}(n_r-l_r)+\frac{4G_mp_r}{(p_r+G_m)}\\ \frac{8G_mm_r(3K_m+4G_m)}{3K_m(m_r+G_m)+G_m(7m_r+G_m)}\\ +\frac{2(k_r-l_r)(2G_m+l_r)}{3(k_r+G_m)}\end{array}\right]. \tag{A10}$$

where, K_m and G_m are the bulk and shear moduli of the matrix which can be written as

$$K_m = \frac{E_m}{3(1-2\upsilon_m)}, \tag{A11}$$

$$G_m = \frac{E_m}{2(1+\upsilon_m)}. \tag{A12}$$

Furthermore, β, α can be obtained from

$$\alpha = \frac{(1+\upsilon_{out})}{3(1-\upsilon_{out})}, \tag{A13}$$

$$\beta = \frac{2(4-5\upsilon_{out})}{15(1-\upsilon_{out})}, \tag{A14}$$

$$\upsilon_{out} = \frac{3K_{out}-2G_{out}}{6K_{out}+2G_{out}}. \tag{A15}$$

where two parameters ξ and ζ show the agglomeration of CNFs as

$$\xi = \frac{V_{inclusion}}{V}, \tag{A16}$$

$$\zeta = \frac{V_r^{inclusion}}{V_r}. \tag{A17}$$

However, the average volume fraction c_r of CNFs in the NFRP is

$$C_r = \frac{V_r}{V}. \tag{A18}$$

Appendix B

The relation of the transformation strain rate ($\dot{\varepsilon t}$) and rate of MVF evolution ($\dot{\xi}$) can be expressed as

$$\dot{\varepsilon}^t = \dot{\xi}\Lambda^t, \tag{B1}$$

in which Λ^t shows the transformation tensor which is

$$\Lambda^t = \begin{cases} \Lambda^t_{fwd} = H(\sigma)\, sgn(\sigma)\dot{\xi} > 0 \\ \Lambda^t_{rev} = \dfrac{\varepsilon^{t-r}}{\xi^r}\dot{\xi} < 0 \end{cases} \tag{B2}$$

where "rev" and "fwd" are reverse and forward transformations, respectively, ε^{t-r}, H and ξ^r show the transformation strain in the reversal point, uniaxial transformation strain for full transformation, and the martensitic volume fraction in reverse transformation, respectively. The transformation function Φ^t related to reverse and forward transformations may be given as

$$\Phi^t = \begin{cases} \Phi^t_{fwd} 0 \le \xi < 1 \dot{\xi} \ge 0 \\ \Phi^t_{rev} 0 \le \xi < 1 \dot{\xi} \le 0 \end{cases} \tag{B3}$$

$$\begin{aligned} \Phi^t_{fwd} &= (1-D)|\sigma| H(\sigma) + \frac{1}{2}\left(\frac{1}{E^M} - \frac{1}{E^A}\right)\sigma^2 \\ &+\rho\Delta s_0 T - \rho\Delta u_0 - f^t_{fwd}(\xi) - Y^t_0, \end{aligned} \tag{B4}$$

$$\begin{aligned} \Phi^t_{rev} &= -(1+D)\sigma\frac{\varepsilon^{t-r}}{\xi^r} - \frac{1}{2}\left(\frac{1}{E^M} - \frac{1}{E^A}\right)\sigma^2 \\ &-\rho\Delta s_0 T + \rho\Delta u_0 + f^t_{rev}(\xi) - Y^t_0, \end{aligned} \tag{B5}$$

For satisfying the thermo-dynamics's second law, the transformation function should be lower than zero as

$$\Phi^t \le 0 \dot{\xi} \Phi^t = 0 \, 0 \le \xi \le 1 \tag{B6}$$

In Eqs. (B4) and (B5), the hardening functions $ffwdt(\xi)$ and $frevt(\xi)$ may be given as

$$f^t_{fwd}(\xi) = \frac{1}{2}a_1(1 + \xi^{n_1} - (1-\xi)^{n_2}) + a_3, \tag{B7}$$

$$f^t_{rev}(\xi) = \frac{1}{2}a_2(1 + \xi^{n_3} - (1-\xi)^{n_4}) - a_3, \tag{B8}$$

where the transformation constants D, $\rho\Delta u_0$, $\rho\Delta s_0$, Y^t_0, a_2, a_1 and a_3 are

$$D = \left.\frac{(C^M - C^A)\begin{bmatrix} H^{cur}(\sigma) + \sigma\partial_\sigma H^{cur}(\sigma) \\ +\sigma(S^M_{1111} - S^A_{1111}) \end{bmatrix}}{(C^M + C^A)[H^{cur}(\sigma) + \sigma\partial_\sigma H^{cur}(\sigma)]}\right|_{\sigma=\sigma^*}, \tag{B9}$$

$$\rho\Delta s_0 = \left.\frac{-2(C^M C^A)\begin{bmatrix} H^{cur}(\sigma) + \sigma\partial_\sigma H^{cur}(\sigma) \\ +\sigma(S^M_{1111} - S^A_{1111}) \end{bmatrix}}{C^M + C^A}\right|_{\sigma=\sigma^*}, \tag{B10}$$

$$\rho\Delta u_0 = \frac{\rho\Delta s_0}{2}(M_s + M_f), \tag{B11}$$

$$Y^t_0 = \frac{\rho\Delta s_0}{2}(M_s - M_f) - a_3, \tag{B12}$$

$$a_1 = \rho\Delta s_0(M_f - M_s), \tag{B13}$$

$$a_2 = \rho\Delta s_0(A_s - A_f), \tag{B14}$$

$$\begin{aligned} a_3 &= -\frac{a_1}{4}\left(1 + \frac{1}{n_1+1} - \frac{1}{n_2+1}\right) \\ &+\frac{a_2}{4}\left(1 + \frac{1}{n_3+1} - \frac{1}{n_4+1}\right), \end{aligned} \tag{B15}$$

where C^A and C^M are the phase diagram constants of austenite and martensite, respectively, A_s, A_f, M_s and M_f are the start of austenitic phase, finish of austenitic phase, start of martensitic phase, and finish of martensitic phase, respectively, $\sigma*$ is the reference stress, n_1, n_2, n_3 and n_4 are the smooth hardening parameters.